Available online at www.sciencedirect.com
ScienceDirect
Acta Materialia 59 (2011) 1121–1133
Acta MATERIALIA
www.elsevier.com/locate/actamat

Texture evolution in commercially pure titanium after warm equal channel angular extrusion

Satyam Suwas [a,*], B. Beausir [b], L.S. Tóth [c], J.-J. Fundenberger [c], G. Gottstein [d]

[a] Department of Materials Engineering, Indian Institute of Science, Bangalore 560 012, India
[b] Institut für Strukturphysik, Technische Universität Dresden, D-01062 Dresden, Germany
[c] Université Paul Verlaine de Metz, Ile du Saulcy, 57045 Metz Cedex 1, France
[d] Institut für Metallkunde und Metallphysik, RWTH, D-52056 Aachen, Germany

Received 21 December 2009; received in revised form 17 October 2010; accepted 18 October 2010
Available online 17 November 2010

Abstract

Texture development in commercially pure titanium during equal channel angular extrusion (ECAE) through Routes A, B_c and C has been studied up to three passes at 400 °C. Textures were measured using X-ray diffraction, while the microstructural analyses were performed using electron back-scattered diffraction as well as transmission electron microscopy. Occurrences of dynamic restoration processes (recovery and recrystallization) were clearly noticed at all levels of deformations. Finally, the textures were simulated using a viscoplastic polycrystal self-consistent (VPSC) model. Simulations were performed incorporating basal, prismatic and pyramidal slip systems as well as tensile and compressive twinning. The simulated textures corroborate well with experimental textures in spite of the occurrence of dynamic restoration processes.

Keywords: Equal channel angular extrusion (ECAE); Titanium; Texture; Dynamic recrystallization; Recovery

1. Introduction

Equal channel angular extrusion (ECAE) is now a well-established process for producing bulk materials with ultrafine grain sizes in the range of 100–500 nm [1]. In this process, a sample is passed through a die with two intersecting channels with equal cross-sectional area and deformed approximately via simple shear at the intersection plane of the channels. The process allows multiple passes and therefore accumulation of shear strain, without significant changes in the dimension of the sample. Variations in the process can be introduced by applying different rotations around the extrusion axis of the sample between multiple passes giving rise to different routes. The most common amongst them is Route A with no rotation between successive passes, Route B with a 90° rotation between the passes (B_c or B_A, depending on whether the rotations have been applied monotonically or alternately clockwise and anticlockwise) [2,3], and Route C, during which a 180° rotation is applied around the axis of the specimen. The process is accompanied by the development of crystallographic textures depending on the processing routes as well as the initial texture [4], each of which could have large bearing on properties of the materials [4,5].

A number of papers have been published on these aspects for various materials, mostly with the ones with face centred cubic (fcc) crystal structure [6–14]; a few have been published on materials with body centred cubic (bcc) [15–20] and hexagonal close packed (hcp) crystal structures [21–26] too. A recent comprehensive review can be found in Beyerlein and Tóth [4]. The evolution of deformation textures in hcp materials depends on the hexagonal c/a ratio. It is well known that deformation textures in hcp materials belong to one of three groups [27]: (i) texture of materials with $c/a < 1.632$ (Ti, Zr, Be, etc.) (multiple slip), (ii) texture of materials with $1.63 < c/a < 1.73$ (no tensile twinning after initial reorientation) (e.g. Mg), and (iii) texture of

* Corresponding author.
E-mail address: satyamsuwas@materials.iisc.ernet.in (S. Suwas).

1359-6454/$36.00
doi:10.1016/j.actamat.2010.10.045

materials with $c/a > 1.63$ (basal slip and twinning) (Zn, Cd). Most of the papers on texture evolution during ECAE of hcp materials are on Mg and its alloys. Only a few studies are reported for ECAE textures in titanium [28–30]. Unfortunately, the literature on microstructural aspects is usually limited to Route A and carried out only up to one or two ECAE passes.

The present study is the first that aims at examining texture evolution during ECAE of titanium using all three important routes, namely A, B_c and C, and up to three passes. A thorough experimental study was carried out using X-ray diffraction (XRD) and electron back-scatter diffraction (EBSD). The experimental textures were simulated using a viscoplastic self-consistent (VPSC) scheme and adequate mechanisms for texture evolutions were proposed. The results of the texture studies were corroborated by microscopic methods at all levels, namely, optical microscopy (OM), scanning electron microscopy (SEM) as well as transmission electron microscopy (TEM).

2. Experimental details

2.1. Material and ECAE experiments

The starting material consisted of a hot rolled plate of commercial-purity titanium (Titan-15). The composition of the starting material is given in Table 1. The plate was annealed at 973 K for 1 h under argon atmosphere in order to remove any residual stress. After annealing, the material was characterized by an equiaxed microstructure with an average grain size ~100 μm, as revealed by secondary electron micrograph (Fig. 1). Specimens with 10 mm × 10 mm square cross section and 100 mm length were machined from the annealed plate. The ECAE experiments were carried out at a cross-head speed of 0.1 mm s^{-1} at room temperature using a Zwick 200 kN screw-driven machine and a die set with rectangular intersection of the extrusion channels without any rounding of the corner region. In brief, the ECAE die was designed to yield a Von Mises strain of ~1.15 during each pass. A detailed description of the ECAE apparatus used in this study can be found in Ref. [31]. The ECAE reference system is shown in Fig. 2. In the first pass, the samples were positioned into the vertical channel so that their previous rolling normal direction coincided with the TD direction of the ECAE die, while their rolling direction (i.e. longitudinal axis) was oriented in the ND direction of the die. Molybdenum disulfide was used for lubrication of the contact surfaces. ECAE experiments were carried out at 400 °C by heating the sample in the die itself. The temperature was controlled using a thermocouple placed very close to the intersection of the two perpendicular channels. The number of ECAE passes was limited to three.

Table 1
Material composition.

Constituent element	Fe	N	H	O	Ti
wt.%	0.07	0.009	0.012	0.10	Balance

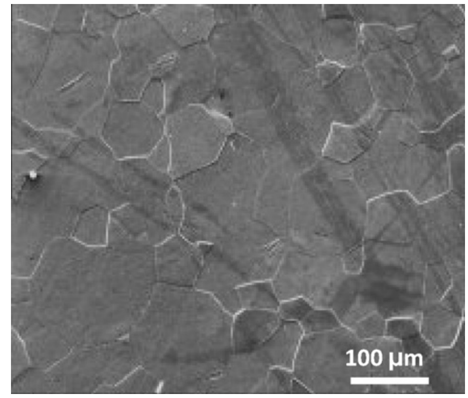

Fig. 1. Microstructure of the starting material as revealed by scanning electron microscope (secondary electron mode) showing equiaxed grains.

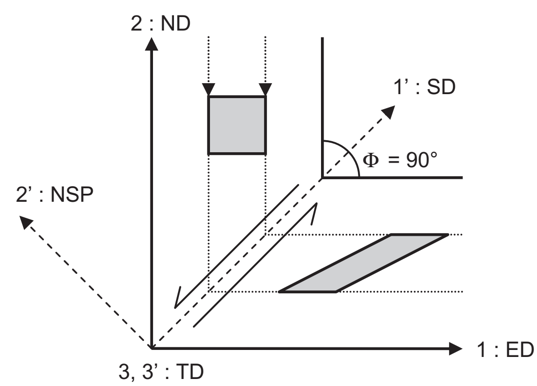

Fig. 2. Scheme of ECAE followed in the present investigation. Here ND, SD, TD, ED represent normal direction, shear direction, transverse direction and extrusion (ECAE) direction respectively. NSP represents normal to shear plane.

2.2. Characterization of microstructure and texture

Texture measurements were carried out by X-ray diffraction (Co Kα radiation, $\lambda = 1.790$ Å). A set of six incomplete pole figures, namely (10.0), (00.2), (10.1), (10.2), (11.0) and (11.2) were recorded on the mid-horizontal plane (ND) of the sample parallel to the direction of extrusion using the Schultz-reflection mode. The ODFs were calculated with the software developed at LETAM using the series expansion method of Bunge [32] up to $l_{max} = 22$ without imposing any sample symmetry. Further, complete pole figures were re-calculated from the ODF data.

The microstructures were examined using a Leo field emission gun scanning electron microscope (FEG-SEM) equipped with EBSD detector and HKL data acquisition system. The EBSD data analysis was carried out using the REDS software developed at Seoul National University [33]. TEM was conducted on a CM 200 Philips operated at 200 kV.

3. Experimental textures

The experimental texture of the starting material is presented in (10.0) and (00.2) pole figures in Fig. 3a and b on the TD projection plane. The shear direction (SD) and the shear plane normal (NSD), as they are oriented during ECAE, are also indicated on the pole figures. They are inclined 45° with respect to ED. The pole figure of the starting material reveals the basal poles located in the TD direction; however, with a significant spread of about 20 and 30° along ND and ED directions, respectively. This kind of texture is quite commonly observed in hot rolled titanium. The pole figures after one-pass ECAE are shown in Fig. 3c and d. The most important ideal texture fibres for simple shear of Ti are also indicated in Fig. 3c and d. They were obtained in the same way as described in Ref. [34] for the case of Mg.

For the ECAE processed materials, two pole figures are shown ((00.2) and (10.0)), in Figs. 4–6. The measured pole figures are presented along with the simulation results for easy comparison. The reference system of all pole figures is the same as defined in Fig. 3.

4. Microstructures

The microstructural features of the ECAE deformed samples were captured through optical micrographs and inverse pole figure maps generated by EBSD, as well as TEM. Figs. 7, 8a and b show optical micrographs of the microstructures after the first and the second passes in Routes A and B_c, respectively. After one-pass ECAE, twinning activity is evident, whereas after the second pass twinning seems much less significant. It can also be seen from these optical micrographs that the deformation is quite heterogeneous throughout the process. In general, bundled structures can be seen around many grains that originate from accommodation strains of the neighbouring grains. The macroscopic shear in the intersection

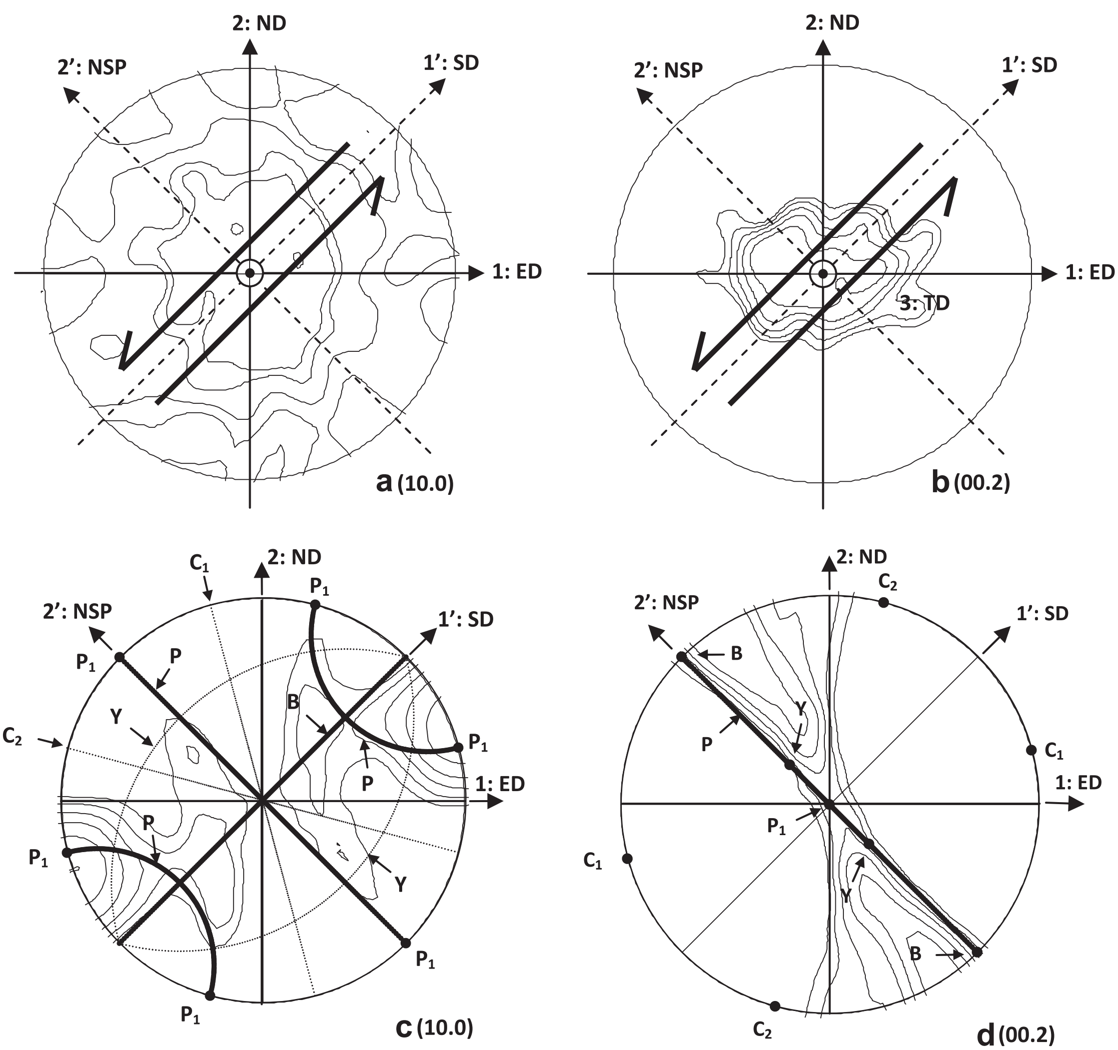

Fig. 3. The initial texture and the shear reference system in (a) (10.0) and (b) (00.2) pole figures. The measured texture after one ECAE pass and the ideal fibres for hcp crystals under simple shear in (c) (10.0) and (d) (00.2) pole figures. The main fibres are identified with thicker lines. Here ND, SD, TD, ED represent normal direction, shear direction, transverse direction and extrusion (ECAE) direction respectively. NSP represents normal to shear plane.

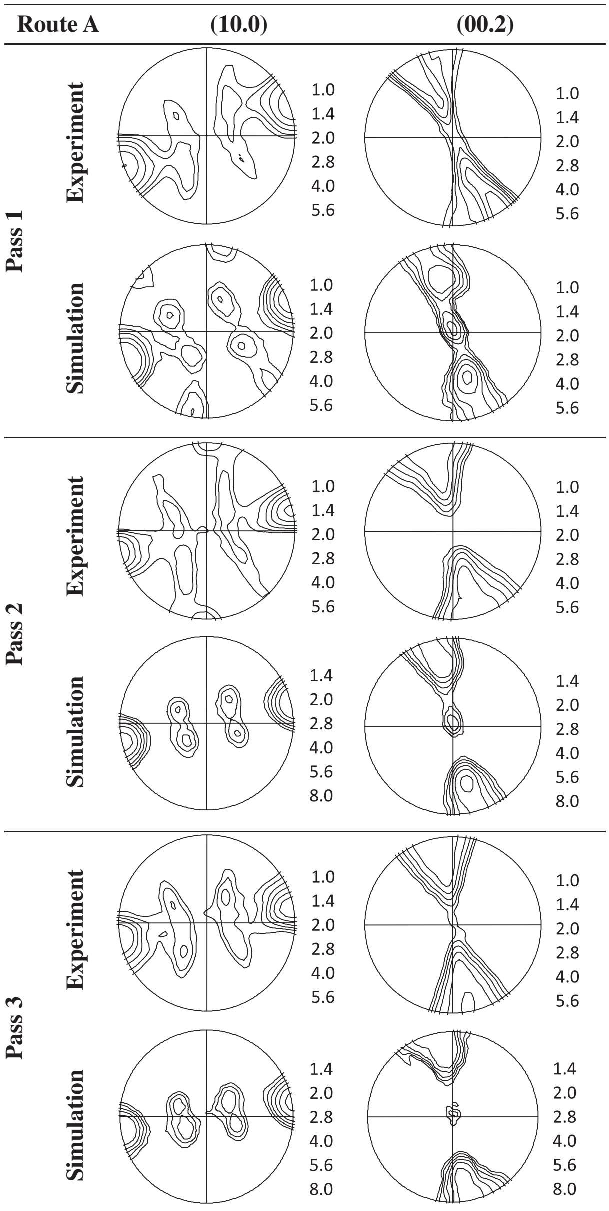

Fig. 4. Texture evolution in Route A as obtained through VPSC simulations and X-ray texture measurements. The reference system in the pole figures is the same as in Fig. 2.

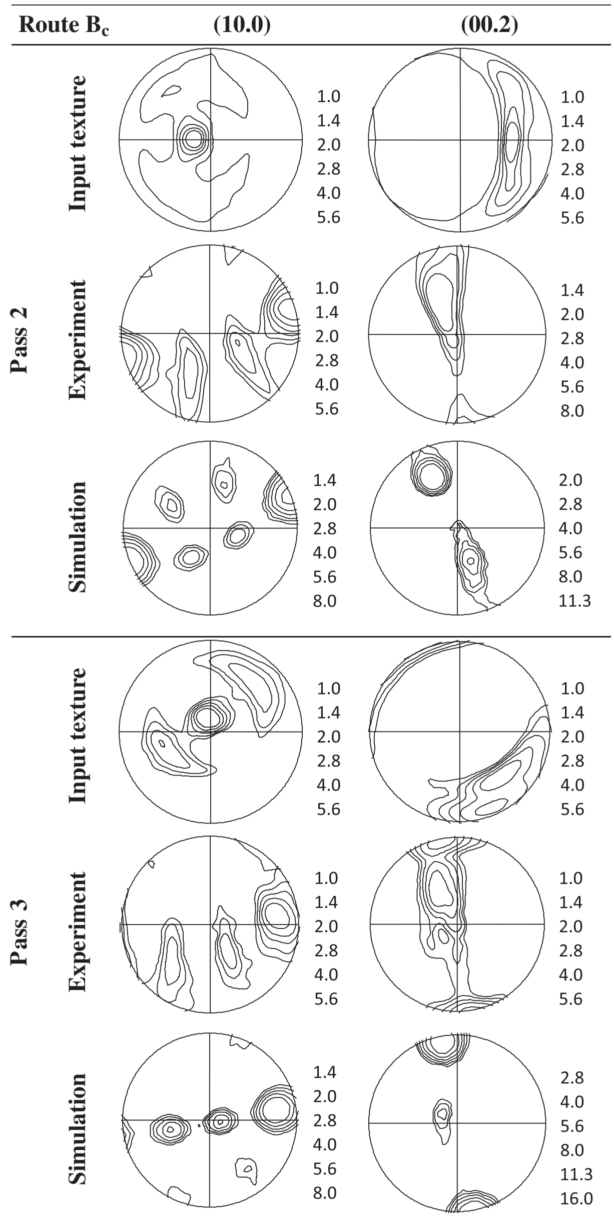

Fig. 5. Texture evolution in Route B_c as obtained through VPSC simulations and X-ray texture measurements. The reference system in the pole figures is the same as in Fig. 2.

plane of the channels elongates the grains in specific directions; one can identify a general orientation of the elongated grain boundaries. The inclination angles of these 'stringers' with respect to the ED direction are in good agreement with the theoretically expected orientations. In the first pass, this angle is about 24°, in the second pass for Route A it is 14°, and for second pass Route B_c, it is again 24°.

Fig. 9 shows the EBSD measurements of the microstructures of the samples obtained after ECAE for all the three routes. In each case, the microstructure is quite heterogeneous, showing refined grains as well as grains that are not fragmented, having small orientation gradients. Within these grains the misorientations do not exceed 5°. Macroscopically, these regions appear like shear bands (see optical micrographs in Figs. 7 and 8). They are inclined at a particular direction with respect to ED. The heterogeneity tends to disappear after the third pass where the fraction of fine grains became reasonably high. Table 2 includes some parameters that characterize the microstructural evolution through different routes of ECAE.

The microstructural features also point towards a dynamic restoration process, which is most probably dynamic recrystallization. Fine equiaxed grains in almost everywhere in the samples are clear indications for such a process. However, the EBSD generated microstructures

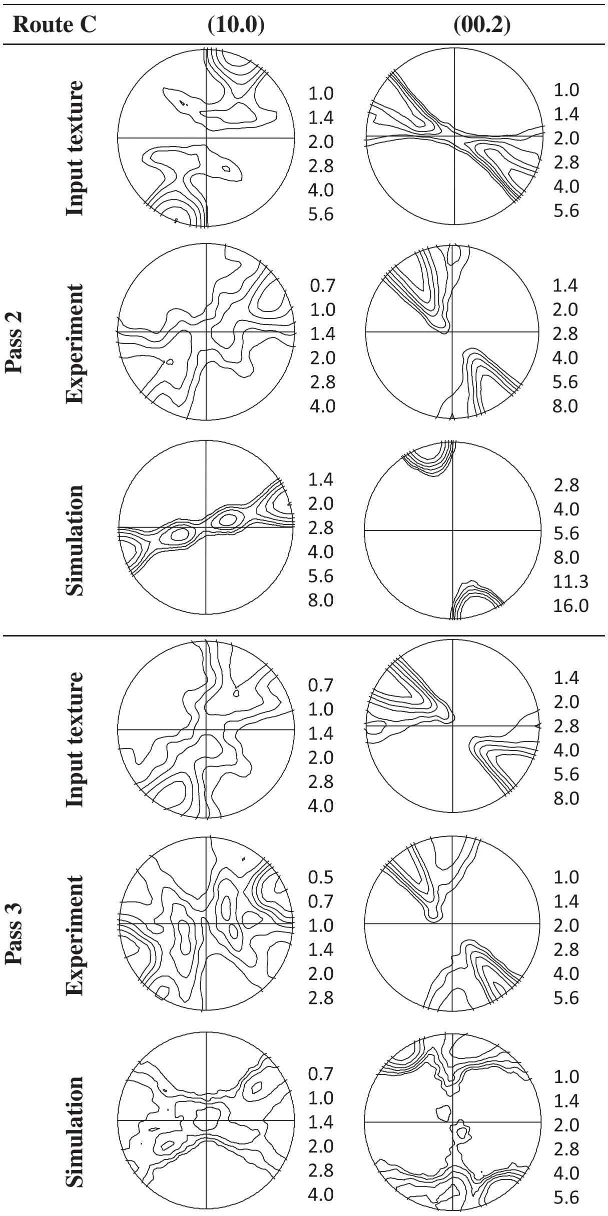

Fig. 6. Texture evolution in Route C as obtained through VPSC simulations and X-ray texture measurements. The reference system in the pole figures is the same as in Fig. 2.

did not reveal the exact nature of the grain refinement process. Therefore, TEM studies were carried out. The TEM micrographs representing the substructure developed after three ECAE passes in all the three routes, A, B_c and C, are shown in Fig. 10. The features are indicative of large deformation followed by recovery in the material. In addition to regions of high dislocation density, elongated parallel bands were observed (Fig. 10a, c, e). Features representing restoration processes (mostly recovery) are also observed. Sometimes these processes lead to configurations like equiaxed subgrains (or recrystallized grains). Deformation twins were seen in the deformed microstructures even after three passes.

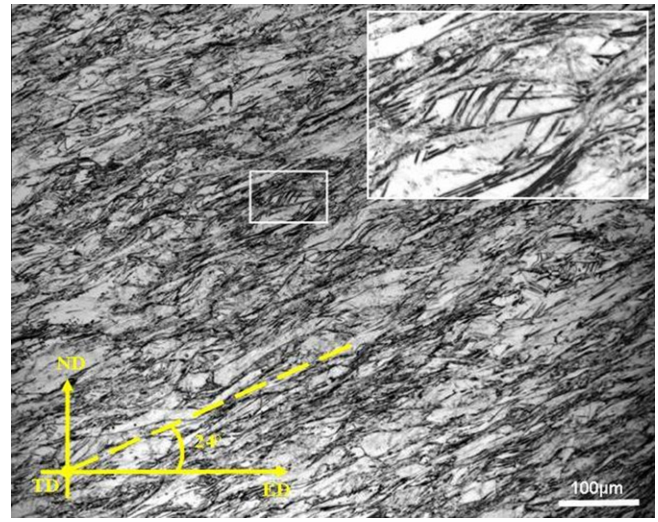

Fig. 7. Optical micrograph showing the occurrence of twinning in the first pass deformed material (magnified view in the insert). The inclination of stringers at 24° to the ECAE direction, as indicated by the broken line, corresponds exactly to the shear imparted during one pass.

5. Texture simulation conditions and results

5.1. Simulation conditions

According to the simple shear model of ECAE, the velocity gradient of simple shear in the plane of symmetry (1′, 2′, 3′ reference system in Fig. 1) is given by:

$$L = \begin{pmatrix} 0 & -\dot{\gamma} & 0 \\ 0 & 0 & 0 \\ 0 & 0 & 0 \end{pmatrix}_{1',2',3'} \tag{1}$$

Here $\dot{\gamma}$ is positive, meaning that the shear direction is actually negative. When this velocity gradient is expressed in the ECAE reference system (1, 2, 3 in Fig. 1), it transforms to:

$$L = \frac{\dot{\gamma}}{2}\begin{pmatrix} 1 & -1 & 0 \\ 1 & -1 & 0 \\ 0 & 0 & 0 \end{pmatrix}_{1,2,3} \tag{2}$$

As can be seen from this second expression, the velocity gradient describes tension in the extrusion direction (1 = ED), compression in the normal direction (2 = ND) and a pure rigid body rotation around the TD axis (3 = TD) [10]. $\boldsymbol{L}$ can be readily incorporated into a polycrystal plasticity model to simulate texture development up to a shear strain of $\gamma = 2$ in each pass.

Simulations were carried out using a viscoplastic polycrystal self-consistent model (VPSC) [35–37]. The Version 7 of the Los Alamos VPSC code was employed [37]. For crystallographic slip, a rate-dependent plastic slip law [38] was employed in the VPSC code:

$$\tau^{s,f} = \tau_0^f \operatorname{sgn}\left(\dot{\gamma}^{s,f}\right)\left|\frac{\dot{\gamma}^{s,f}}{\dot{\gamma}_0}\right|^m = \tau_0^f \frac{\dot{\gamma}^{s,f}}{\dot{\gamma}_0}\left|\frac{\dot{\gamma}^{s,f}}{\dot{\gamma}_0}\right|^{m-1} \tag{3}$$

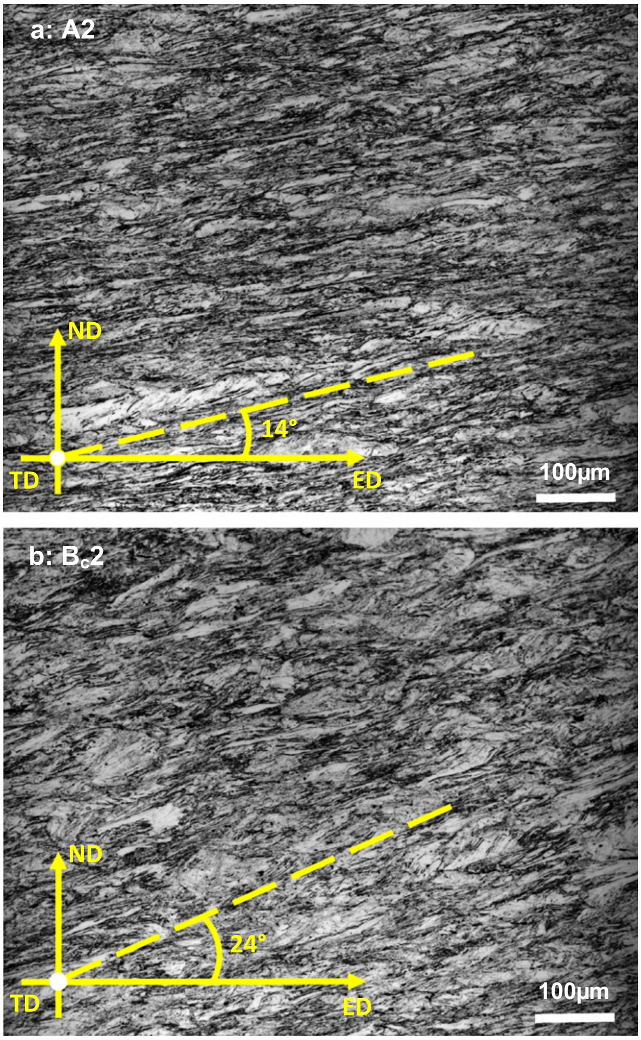

Fig. 8. Optical micrographs of the second pass: (a) Route A and (b) Route B_c, deformed materials. In (a) the inclination of stringers at 14° to the ECAE direction, as indicated by the broken line, corresponds to the shear imparted during two passes, while in (b) the broken line corresponds to shear imparted during one pass.

Here $\tau^{s,f}$ is the resolved shear stress in the slip system indexed by 's' of the slip system family indexed by 'f', $\dot{\gamma}^{s,f}$ is the slip rate, the τ_0^f value is the reference stress level (at which the slip rate is $\dot{\gamma}_0$), and m is the strain rate sensitivity index. The reference shear rate $\dot{\gamma}_0$ is supposed to be the same for all slip systems. The slip systems are grouped into "families". The index f is used to represent a particular family. The main slip families in hexagonal structures are basal, prismatic and pyramidal slips. It is assumed here that the reference shear stress τ_0^f is the same for a given slip system family, but can be different from one family to another.

In order to capture reorientation by twinning, the predominant twin reorientation (PTR) model proposed by Tomé et al. [39] has been implemented in VPSC scheme. In this model, a grain is fully oriented to the orientation of its predominant twin system when the volume fraction associated with the activity of this twin exceeds a threshold value. As a consequence, grains either retain their original matrix orientation or fully adopt the orientation of its predominant twin, but in either case they remain homogeneous. The PTR model thus homogenizes the actual twin-matrix microstructure over the polycrystal as in a rule of mixtures approach.

An important issue in hexagonal materials is the relative contribution of the different slip families (here: basal, prismatic and pyramidal) and of twinning (here: compressive and tensile twins) to the total deformation. The set of relative reference strength which led to the best simulation results is given in Table 3. It is to be noted here that the simulations assume $\tau_0^{prism.} > \tau_0^{basal}$, which needs explanation. Although single crystal measurements show that the major slip system in titanium is the prismatic one, the situation can be different in polycrystals. Actually, polycrystal simulations show that good matching with experiments can be obtained only if basal slip is much easier than prismatic slip. This can be explained by the fact that the initially soft prismatic systems harden rapidly due to slip on other slip systems and most of all, by twinning. It will be shown below that twinning is mostly active during the first pass and the twin lamellas increase the slip resistance in the prismatic planes.

At relatively high homologous testing temperature (T/T_m 0.3, T_m melting temperature), the strain rate sensitivity parameter m was chosen to be 0.1. The initial texture was discretized into 2000 grain orientations and was used as input for the first pass. The simulations were performed continuously, i.e. in each subsequent pass the previously simulated texture was the input texture. No hardening was imposed for crystallographic glide, but linear self-hardening was employed on the twinning modes according to a modified Voce law [37]:

$$\hat{\tau}^{s,f} = \tau_0^{s,f} + \left(\tau_1^{s,f} + \theta_1^{s,f}\Gamma\right)\left(1 - \exp\left(-\Gamma\left|\frac{\theta_0^{s,f}}{\tau_1^{s,f}}\right|\right)\right) \tag{4}$$

here Γ is the accumulated slip in the grain; $\tau_0^{s,f}$, $\theta_0^{s,f}$, $\theta_1^{s,f}$ and $\left(\tau_0^{s,f} + \tau_1^{s,f}\right)$ are the initial critical resolved shear stress (CRSS), the initial hardening rate, the asymptotic hardening rate and the back-extrapolated CRSS, respectively. This hardening law was employed only for the purpose of suppressing twinning activity at shear deformations larger than $\gamma = 2$ (see Section 6). Table 3 includes all parameters employed during the simulation. Concerning the reference system for the Euler angles of the grain orientations, a Cartesian system was attached to the unit cell of the hexagonal crystal structure so that the axes x_1, x_2 and x_3 of the testing geometry were parallel to the crystallographic [10.0], [11.0] and [00.2] directions, respectively. The results of the simulations are presented in Figs. 4–6 in (10.0) and (00.2) poles figures along with the experimental textures.

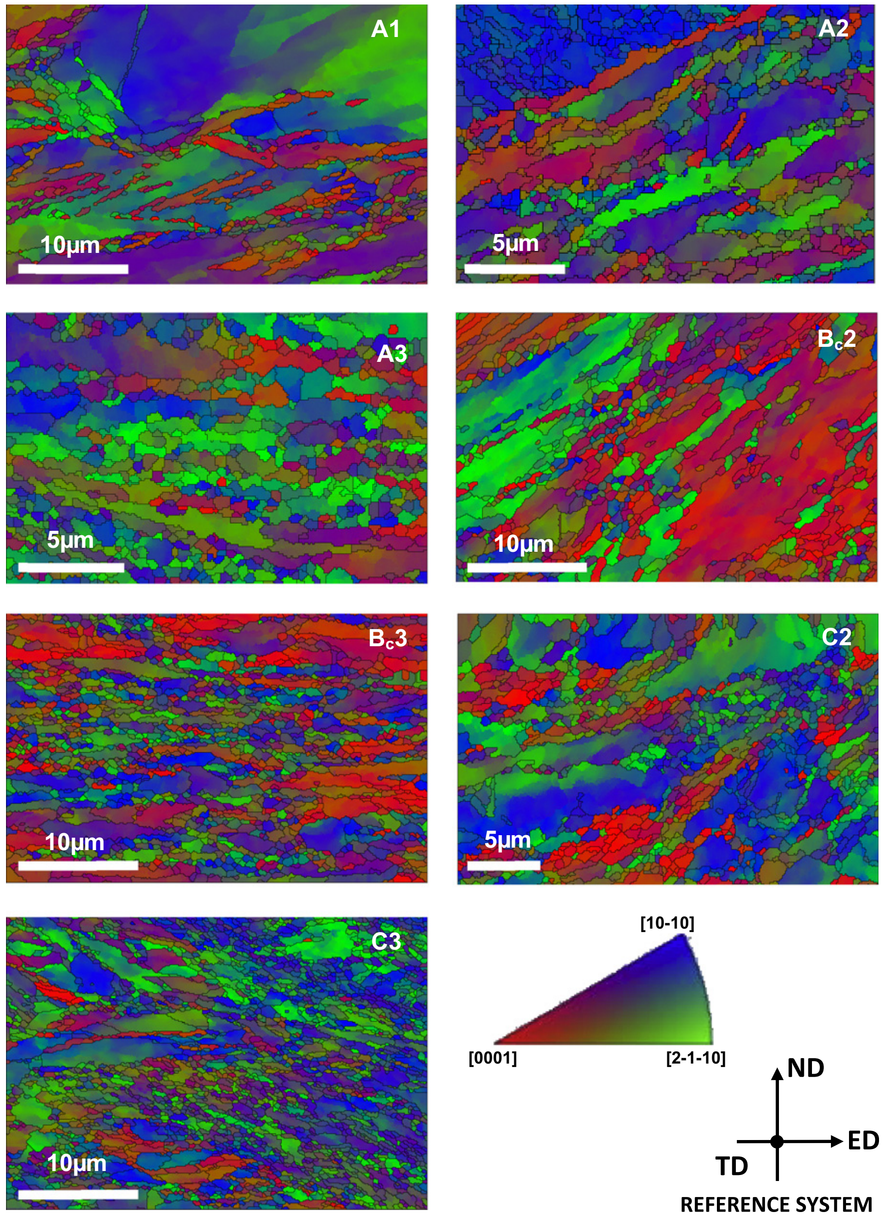

Fig. 9. EBSD generated microstructures (inverse pole figure maps of the TD axis) of the investigated material. The code in the top right corner includes the processing route and the pass number. The colour code and the reference system for the EBSD measurements are provided. (For interpretation of the references to colour in this figure legend, the reader is referred to the web version of this article.)

Table 2
Microstructural parameters obtained from the EBSD investigation. (The average grain size is calculated from the equivalent circle surface.)

Processing route	No. of passes	Average grain size	Aspect ratio
A/B_c/C	1	870 nm	1.96
A	2	727 nm	1.80
A	3	658 nm	1.73
B_c	2	876 nm	1.52
B_c	3	708 nm	1.53
C	2	778 nm	1.60
C	3	711 nm	1.91

5.2. Simulation results

As can be seen in Fig. 4, for all passes of Route A, the grain orientations accumulate before the B and P fibre from the right side (see Fig. 3 for the locations of the ideal fibres). Thus, they form a fibre that appears in rotated position from both the B and P fibre; the fibre is clearly seen in the [00.2] pole figures. The B fibre appears very broad at the periphery of the pole figure. All textures obtained in Route A are centro-symmetric, that is, they obey the symmetry of the simple shear process which has a twofold symmetry around the TD axis, which is in the centre of the pole figures. The simulations reproduce the basic features of the experiments.

Fig. 5 displays the simulated and experimental textures in materials processed through Route B_c. For this route as well as for Route C, the input textures are also shown for each pass, which is the texture of the previous pass rotated by $-90°$ around the TD axis and also rotated

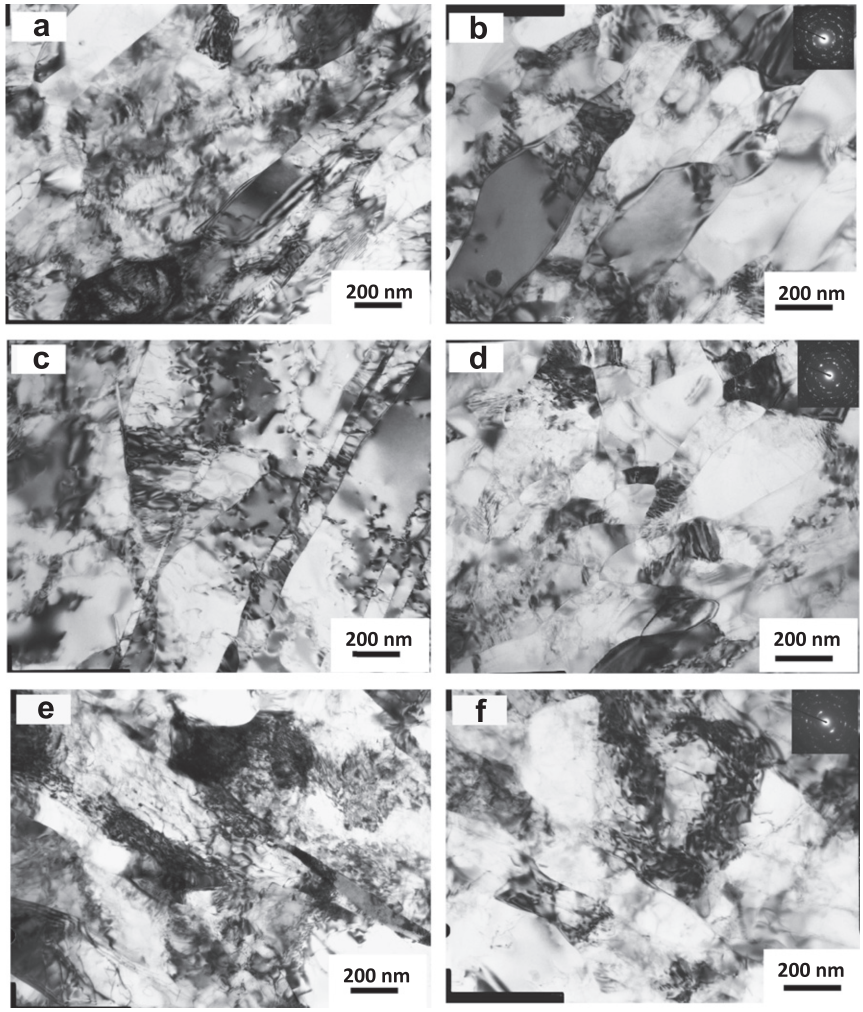

Fig. 10. TEM micrographs obtained from the mid thickness sections of the Ti samples. The foils were extracted from the TD planes of the three-pass deformed samples following (a, b) Route A, (c, d) Route B_c and (e, f) Route C.

Table 3
Relative reference strength and hardening parameters.

Modes	τ_0^f	τ_1^f	$\theta_0 = \theta_1$
Basal	0.5	–	–
Prismatic	4.0	–	–
Pyramidal $\langle c + a \rangle$	6.5	–	–
Tensile twin	2.4	0	1
Compressive twin	3.4	0	1

around the sample axis according to the route. In this way, the effect of simple shear during the next pass can be directly seen in the texture. The distinguishing feature of the textures in Route B_c is that they are not centro-symmetric. This is due to the change of the direction of the shear with respect to the sample as the latter is rotated around its longitudinal axis by +90° after each pass. Nevertheless, the textures after two and three passes with Route B_c are not too different from each other. The simulated texture of Route B_c processed samples reproduce faithfully the experimental texture in terms of locations of the components. Nevertheless, the intensities of the simulated textures are somewhat higher than the corresponding experimental textures.

The textures obtained in Route C are displayed in Fig. 6. One would expect that after two passes in Route C, the initial texture should be reproduced (because of the opposite shear in the second pass with respect to the first pass). However, by comparing Fig. 3a and b with the two-pass texture in Fig. 6, enormous differences in the texture of the two-pass deformed material and the initial texture can be seen. Interestingly, the second-pass texture resembles very much the first-pass texture. These features are well reproduced by the simulations, except for the third pass. Another observation is that there are unusually large rotations of the textures during a single pass in the Route C. They can be clearly identified by comparing the "input' textures with the deformed ones (designated as "experiment") in Fig. 6. The form of the deformation textures permit us to clearly identify an anticlockwise rotation of about 150–160° around the TD axis with respect to the input texture.

6. Discussion

The results of experiments and simulations will now be discussed for each of the processing routes with reference to adequate support from microstructural observation.

6.1. Slip and twinning activity

The relative activity of the different slip families as well as twinning for the three routes is presented in Fig. 11 as obtained from the simulations. In the figure, the tensile twin (TT) and compressive twin (CT) fractions represent the sum of the volume fraction of twins in a grain over all grains. The reorientation of grains by twinning starts when a threshold value A^{th1} in any given twin system is reached (in the present investigation, $A^{\text{th1}} = 15\%$) and rapidly raises the threshold to a value around $A^{\text{th1}} + A^{\text{th2}}$ (where $A^{\text{th2}} = 50\%$). As can be seen, basal slip is the most active followed by prismatic and finally the pyramidal $\langle c + a \rangle$ slip. This observation corroborates the findings of Yapici and Karaman [40], who analysed the ECAE textures in a number of hcp materials and found that texture evolution during ECAE of hcp materials is commonly attributed to basal slip irrespective of material or processing variables. Twinning activity is also relevant in the first pass leading to an ~50% accumulated volume fraction of compression twinned grains and 30% of tensile twinned grains. Then twinning is suppressed in subsequent passes because of the imposed hardening for twinning, see the imposed hardening characteristics in Eq. (3) and Table 3. An interesting feature of the slip system activity in passes two and three is that when basal slip increases then prismatic slip decreases and vice versa. The two curves, basal and prismatic, are very symmetric for all the routes. This is a consequence of the very low activity of the third slip system, namely pyramidal $\langle c + a \rangle$, as well as twinning. It is to be noted here that Fig. 11 shows the relative activity for slip. When only two families are active, it is necessary

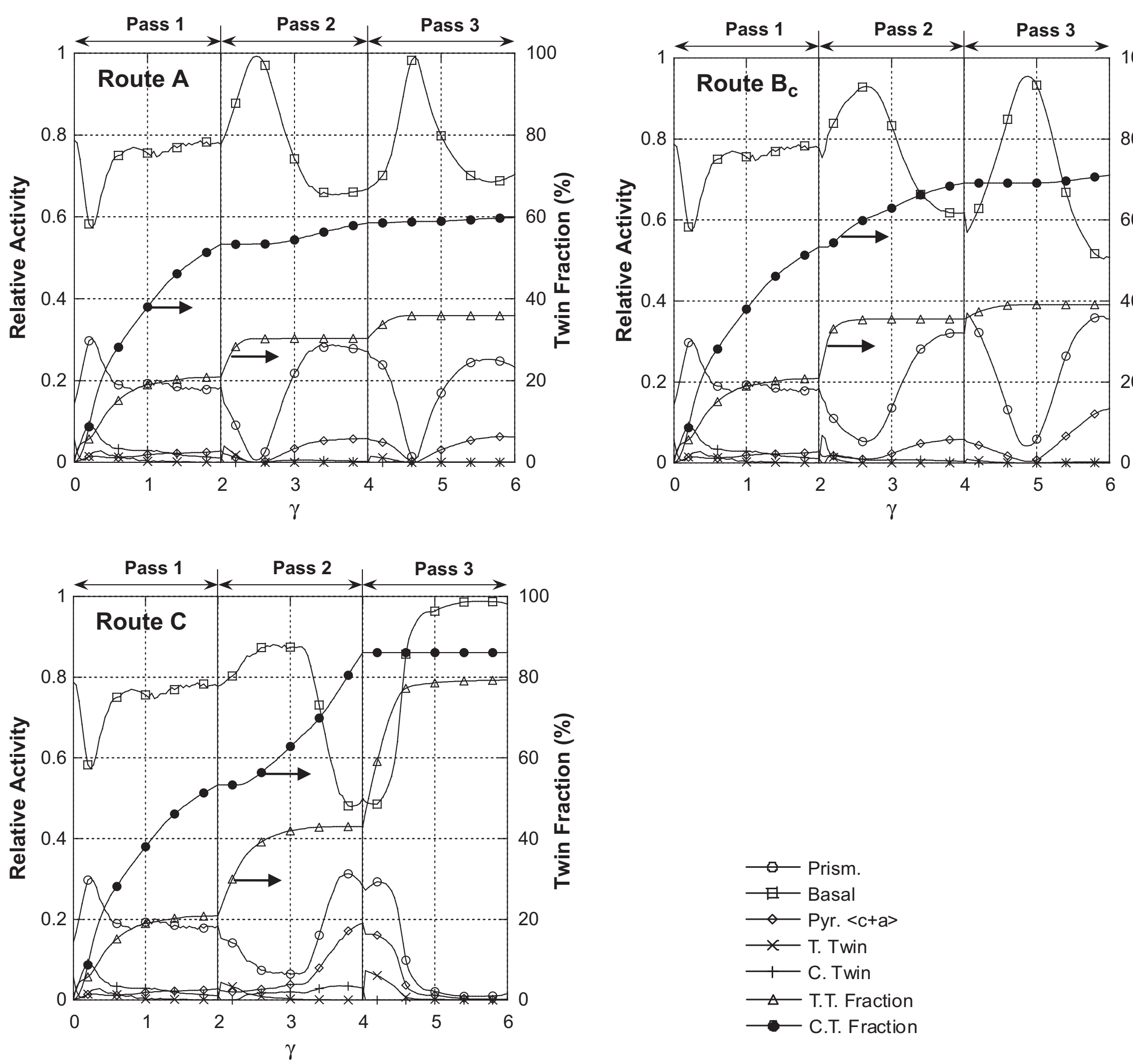

Fig. 11. Relative activities of slip and twinning as well as twin volume fractions during ECAE processing through Routes A, B$_c$ and C, as calculated by PTR model, for details refer to text. Here T and C twins represent compressive and tensile twins, while TT and CT fractions stand for their respective volume fractions.

that they change exactly in an opposite way, simply because they always have to produce the same amount of total imposed deformation.

It is important to recall here that the relative strengths of the different slip and twinning families were chosen in the simulations in such a proportion that the experimental textures were best reproduced. Moreover, the same relative strengths were used for simulating the texture for all three passes. It has been realized through the present simulations that the high activity of basal slip is a very important element in the ECAE textures of titanium; however, prismatic is also very significant. It is to be mentioned here that in the case of Mg, the experimental textures could be reproduced with negligible contribution from prismatic slip [22]. Twinning also seems to be a contributing deformation mechanism (although minor) during ECAE of titanium as will be discussed more below in the section on microstructures.

6.2. Route A

During the first pass of ECAE, the orientations approach the ideal fibres that are characteristic to simple shear textures of hcp materials [22]. After one-pass ECAE deformation, the maximum intensity is located at a distance of about 5° from the ideal positions (see Fig. 3). The simulated texture agrees well with the experimental ones, with regard to both positions and intensities, when twinning is accounted for (see Fig. 4). However, when twinning is left out from the simulation (Fig. 12), the texture becomes much sharper. Another effect is a shrinking of the spread in the simulation that can be observed at the periphery of the (00.2) pole figure. This effect is clear by comparing the simulated textures obtained with and without twinning in Figs. 4 and 12 for the first pass. It can be seen that the grain orientations that give rise to the intensities near the ND direction disappear when twinning is suppressed. Thus, the effect of twinning is to enhance the intensity near the ND axis, thus producing a large orientation spread and a general decrease of the texture strength. They are both important elements in the reproduction of the experimental texture by simulations. Nevertheless, the optical micrographs show the presence of twins (see the insert of the optical micrograph in Fig. 7).

During the second and third passes, the texture remains nearly the same after each pass; however, it is the result of a large evolution. Namely, for a subsequent ECAE pass in Route A, the sample needs to be rotated by −90° around the TD axis before it is re-inserted into the die. Such a physical rotation introduced during experiment brings the previously formed textures to a new position at 90°. The plastic deformation imposed during ECAE process further rotates the textures globally by +90° around TD so finally the same locations are reached as before. The simulation incorporating this scheme captures the main features of the experimental textures. Twinning activity is reduced in the simulations from the second pass onwards – assuming a Voce type hardening also for twinning (see above). Nevertheless, some twins could still be seen in the microstructures in a few large grains, see the optical micrograph shown in Fig. 8a and b. They are probably twins that were formed already in the first pass and just deformed during subsequent passes.

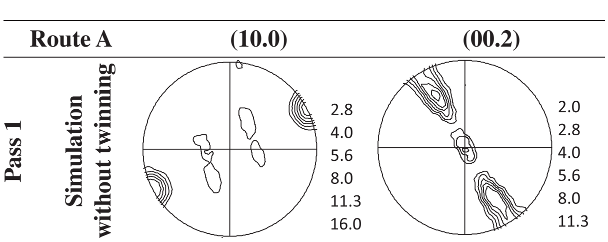

Fig. 12. Simulated texture without twinning after one pass of ECAE.

6.3. Route B_c

The interpretation of the texture development in Route B_c is much more complex than in Routes A or C, because of the orthogonal changes in the strain path after every pass. Contrary to Route A, the textures obtained are not the same after the second and third passes. This is why the pole figures are also plotted after incorporating adequate rotations to represent the "input" textures in Fig. 5, that is, when the sample is re-inserted into the vertical channel of the die. As can be seen in the figure, these input textures are significantly different, which is actually the reason for the differences in the output textures. The simulated textures are in relatively good agreement with experiments, which is achieved with crystallographic slip only, meaning that deformation twinning does not affect texture significantly after the first pass. Nevertheless, there is some significant activity of twinning in the simulations just at the beginning of the extrusion in the second pass, see Fig. 8a, which can be explained by the reorientation of grains that did not twin in the first pass into a favourable twinning position due to the rotation of the sample according to the routes.

6.4. Route C

One of the main features of the Route C textures, see Fig. 6, is that there are unusually high lattice rotations during extrusion; they amount up to 160° in one single pass (compare to texture analysis in previous sections). Knowing that during a shear strain of $\gamma = 2.0$ the imposed rigid body rotation is only 57.3°, the observed lattice rotation is about three times higher. In principle, the lattice rotation needs not to be limited by the rigid body rotation as was actually shown recently [22]: in certain grain orientations, the lattice spin can be twice as high as the rigid body spin. This occurs for such textures where shearing is applied perpendicular to the basal plane [22]. The modelling of such large rotations in that study was based on the Taylor model, whereas in the present simulations a VPSC code was used. Thus, it can be suspected that shape effects can play a specific role in the lattice rotation. Actually, in the self-consistent model, the grains can deform differently from the macroscopically imposed state. This difference means that the grain shape axes can vary from grain to grain. Therefore, the rigid body rotation, which is the anti-symmetric part of the local (grain) velocity gradient, can be larger or smaller than the macroscopic one. As the lattice rotation is the difference between the locally imposed velocity gradient and the velocity gradient of plastic slip, the lattice rotation is affected by the local deformation of the grain. This local deformation determines the evolution of the grain shape as well. Actually, in Route C, the shape of the grain is reversed to its original shape after every second pass, in contrast to Route A where it rotates monotonically. A large amount of grain-shape-axis rotation happens in the first pass. Consequently, in the second Route C pass, when the shear is reversed, there is again the same amount of grain-shape-axis rotation in the opposite direction. One can verify in the original paper of the self-consistent model by Molinari et al. [35] that actually the rotation of the grain-shape axis plays an important role in the lattice rotation of the crystal (see Eq. (35) in Ref. [35]). In each pass, the rotation of the grain-shape axis takes place in the direction of the applied shear and therefore enhances the lattice rotation. This is why the texture rotates by such a large magnitude. The current simulation emphasizes the importance of using polycrystal plasticity models that are capable of taking into account the effect of grain shape in the modelling of lattice rotation.

The other well known experimental fact in Route C is the non-perfect reversibility of the texture after the second pass. This is the case also in the present experiments. The pass-two texture is different from the initial texture. However, the third pass texture is very similar to the first-pass texture; compare Fig. 6 with Figs. 4 or 3. This particular experimental observation needs interpretation. The explanation can be given based on two aspects: the grain shape and the initial texture. During the first pass, the initial grain shape is equiaxed. The evolution of the grain shape influences the lattice rotation. However, during the second pass, when the shear is reversed, the influence of the grain-shape-axis rotation in the resultant lattice spin is different, too. Thus, even if the imposed velocity gradient is exactly reversed, the starting grain shape in the second pass is not equiaxed but very much elongated. Consequently, the lattice spin will not be exactly reversed, due to the contribution of the grain shape in the lattice rotation. Therefore, the texture evolution is not exactly inverted and the initial texture will not be recovered. (It would be exactly recovered in Taylor modelling where there is no effect of grain shape.) Nevertheless, the simulated texture in the second pass of Route C is quite different from the experimental one, see Fig. 6. However, it is not equal to the initial one either. This deviation is probably due to twinning. As it was shown above, twinning is very active in the first pass but not active in subsequent passes. However, the twinned grain volumes remain in the grains and will affect the shape evolution of the grains in a very significant manner. This can be the reason for the differences between the experimental and simulated textures. It is to be noted here that in the present modelling a relatively simple twinning model was employed; the used predominant reorientation twinning scheme causes a grain to become completely replaced by its twin in the case of a high twinning activity. More sophisticated twinning models may give a better approximation of the real twinning process in order to account for the effect of twinning on texture development in a more physical manner.

Now the similarity between the textures after the first pass and the third pass of Route C can be explained as follows. After the first pass, the grains have assumed already an elongated shape, and a texture specific to ECAE shear has developed. During the second pass, the initial grain shape is recovered and again a texture appears that is an ECAE (shear type) texture, see Fig. 6. The reasons why it is different from the initial texture were discussed above. In the third pass the same grain shape is achieved as after the first pass from an initial texture that is not too far from the starting texture, thus a similar texture develops.

6.5. Slip vs. twinning

Shin et al. [29] studied the evolution of microstructures during ECAE of CP titanium deformed in all the three routes followed in the present investigation namely, A, B_c, and C. They have also found that twinning plays an important role in the first pass. During the subsequent passes, Shin et al. [29] realized that the deformation mechanism changed to dislocation slip on a system which depended on the specific route. For Route A, the deformation was controlled by basal slip and twinning, while for Route B_c, prismatic slip was the main deformation mechanism. The results of the present investigation do not corroborate the above findings by Shin et al. exactly. This could be due to the difference in ECAE temperatures. In our experiments the material was deformed at the temperature ~400 °C, while Shin et al. have carried out ECAE at 350 °C. Moreover, in titanium, the twinning is also dependent on chemistry, mainly on the oxygen content of the material as well as the grain size and texture of the initial materials.

The simulations in the present investigation also indicate the increased activity of prismatic slip during Route B_c compared to Route A, see Fig. 11. The specific slip system was strongly dependent on the processing route, i.e. Routes A, B_c, or C. However, in contrast to the observations of Shin et al. [29], the results of the simulations in the present investigation indicate a predominant basal slip during the three routes. It is to be mentioned that twinning seems to influence texture significantly during ECAE of fcc materials [14,41]; however there is no such documentation on the role of twinning on texture formation during ECAE of hcp metals.

6.6. Dynamic recovery vs. recrystallization

The microstructures obtained through inverse pole figure maps clearly reveal the presence of large number of equiaxed grains. This indicates that the material underwent restoration, predominantly recovery and partial recrystallization. This could apparently influence texture as reported for various other materials [41–43]. It is generally tempting to call the microstructural features recrystallized grains; however, owing to the fact that it is difficult to separate these two effects in EBSD generated microstructures because the pattern quality as well as aspect ratio remains similar for both the situations, it is not conclusive. The recovered/recrystallized grains were quantified following a criterion of grain average misorientation (GAM) <1° and grain size <2 μm. Fig. 13 shows the fraction of equiaxed grains with the number of passes for each of the processing routes as obtained from EBSD measurements.

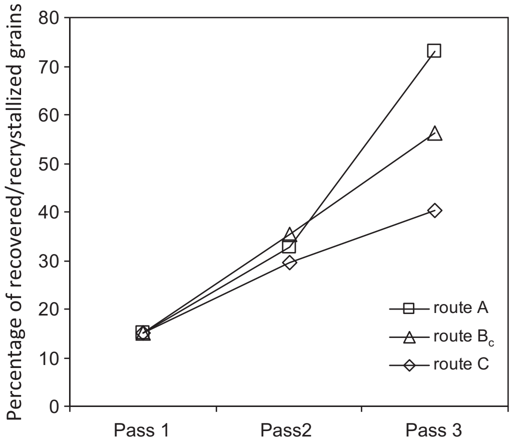

Fig. 13. Fraction of fine and nearly equiaxed grains resulting from dynamic recovery/recrystallization process, as obtained on the basis of grain average misorientation (<1°) and grain size (<2 μm) criteria.

TEM micrographs, however, indicate a recovered microstructure, rather than recrystallized (Fig. 10) for all three routes, even after three passes. The texture also corroborates the above observation. It was shown that the textures could be reproduced through crystal plasticity based simulation, without taking into account any recrystallization event. This could be due to two effects: (a) the material has undergone dynamic recovery during ECAE, i.e. without significant change in orientation, and/or (b) dynamic recrystallization processes did not change the texture. Fig. 14 displays a relatively larger area EBSD scan, where the deformed grains have been separated from recovered/ recrystallized grains on the basis of grain orientation

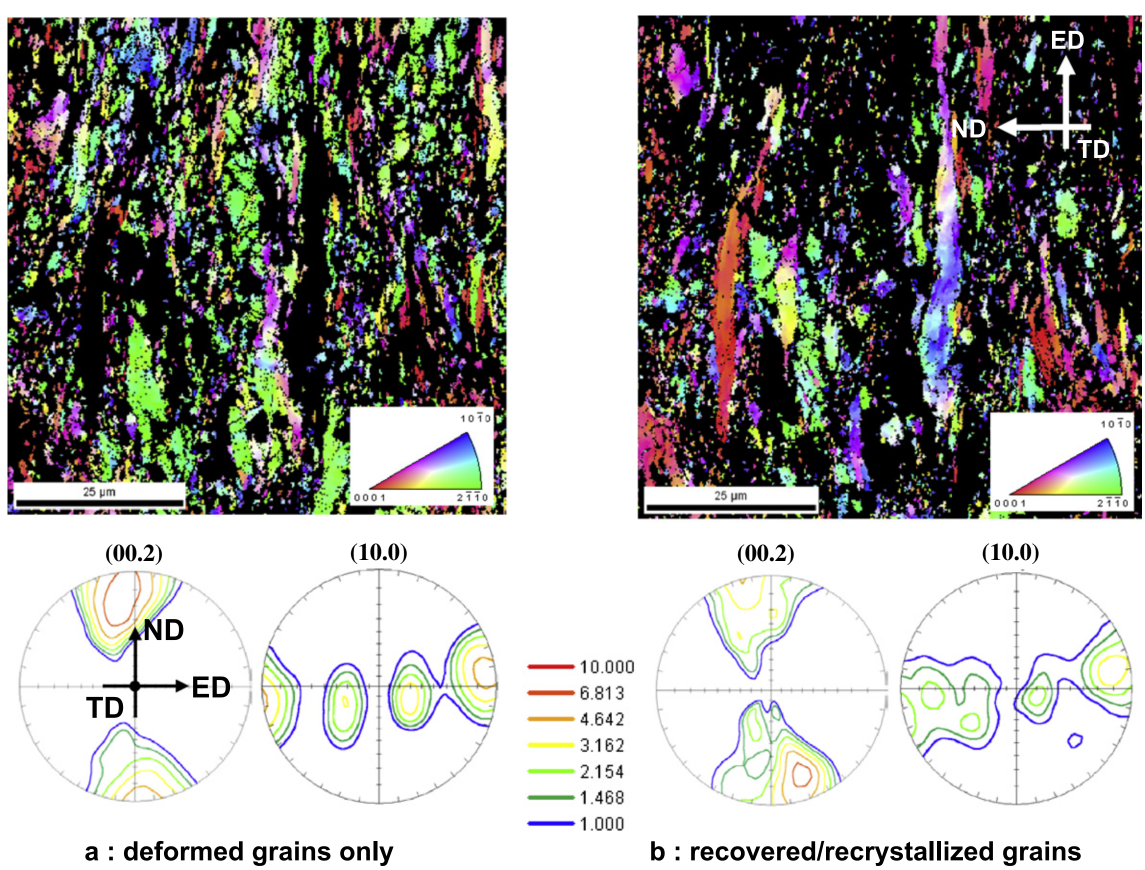

Fig. 14. Regions of microstructures separately shown for (a) deformed and (b) recovered/recrystallized regions for the three-pass (Route B_c) deformed material. The inverse pole figure maps relate to the TD axis, reference axes depicted in (b). The maps were obtained using the TSL software. The recovered/recrystallized grains were separated using the grain orientation spread (GOS) criterion. The corresponding textures are plotted in (00.2) and (10.0) pole figures. The reference system for both the pole figures is the same, as shown in (a).

spread (GOS). The textures were calculated separately for both features, and the results indicate that no texture change occurred during the restoration of the grains. This supports the assertion that the material did not undergo discontinuous dynamic recrystallization during ECAE; rather, it underwent extensive dynamic recovery, resulting in almost similar textures for both the deformed and restored parts.

7. Conclusions

Equal channel angular extrusion of CP titanium was carried out at 400 °C following Routes A, B_c and C up to three passes. Crystallographic textures were measured, simulated and explained on the basis of ideal orientations of shear textures in hcp materials. Based on the obtained results, the following conclusions can be formulated:

1. ECAE of commercially pure titanium leads to the formation of strong textures, characteristic of each route of ECAE deformation.
2. The development of the texture could be well-reproduced using viscoplastic self-consistent simulations for all the routes by using the same ratios of the CRSS, that is: $\tau_0^{basal} = 0.5$, $\tau_0^{prism.} = 4.0$, $\tau_0^{pyr.\langle c+a\rangle} = 6.5$. Basal slip is found to be the predominant deformation mechanism for ECAE irrespective of the routes.
3. The VPSC simulations revealed that twinning was active during the first pass deformation, beyond which its contribution to the deformation was minor.
4. Up to the third pass, the microstructures could be well described as deformation microstructures having undergone recovery.

Acknowledgements

Satyam Suwas is grateful to the Alexander von Humboldt foundation for the research fellowship granted to him, during which this work was carried out. He personally acknowledges the help rendered by Dr. Weiping Hu at RWTH, Aachen in TEM investigation and Nilesh Gurao at IISc, Bangalore in re-analysis of the EBSD data. The authors also acknowledge Prof. K.-H. Oh, Seoul National University and Dr. D.-I. Kim, Korea Institute of Science and Technology, Seoul, for providing the REDS software. B. Beausir is grateful for the Alexander von Humboldt research foundation for his research fellowship.

References

[1] Segal VM. Mater Sci Eng A 1995;A97:157.
[2] Valiev RZ. Mater Sci Eng A 1997;A234–236:59.
[3] Segal VM. Mater Sci Eng A 1999;A271:322.
[4] Beyerlein IJ, Toth LS. Prog Mat Sci 2009;54:427.
[5] Valiev RZ, Langdon TG. Prog Mat Sci 2006;51:881.
[6] Alexandrov IV, Zhu YT, Lowe TC, Islamgaliev RK, Valiev RZ. Metall Mater Trans A 1998;29A:1047.
[7] Zhu YT, Lowe TC. Mater Sci Eng A 2000;A291:46.
[8] Terhune SR, Swisher DL, Oh-Ishi K, Horita Z, Langdon TG, McNelley TR. Metall Mater Trans A 2002;33A:2173.
[9] Gholinia A, Bate P, Prangnell PB. Acta Mater 2002;50:2121.
[10] Tóth LS, Arruffat-Massion R, Germain L, Baik SC, Suwas S. Acta Mater 2004;52:1885.
[11] Suwas S, Arruffat-Massion R, Tóth LS, Fundenburger J-J, Eberhardt A, Skrotzki W. Metall Mater Trans A 2006;37A:739.
[12] Suwas S, Tóth LS, Fundenburger J-J, Eberhardt A, Skrotzki W. Scripta Mater 2003;49:1203.
[13] Skrotzki W, Scheerbaum N, Oertel C-G, Arruffat-Massion R, Suwas S, Tóth LS. Acta Mater 2007;55:2013.
[14] Beyerlein I, Tóth LS, Tomé CN, Suwas S. Philos Mag 2007;87:885.
[15] De Messemaeker J, Verlinden B, Van Humbeeck J. Acta Mater 2005;53:4245.
[16] Bhowmik A, Biswas S, Suwas S, Ray RK, Bhattacharjee D. Metall Mater Trans A 2009;40A:2729.
[17] Gazder AA, Dalla Torre F, Gu CF, Davies CHJ, Pereloma EV. Mater Sci Eng A 2006;415:126.
[18] Li SY, Gazder AA, Beyerlein IJ, Pereloma EV, Davies CHJ. Acta Mater 2006;54:1087.
[19] Li SY, Gazder AA, Beyerlein IJ, Davies CHJ, Pereloma EV. Acta Mater 2007;55:1017.
[20] Gazder AA, Li S, Dalla Torre FH, Beyerlein IJ, Gu CF, Davies CHJ, et al. Mater Sci Eng A 2006;437:259.
[21] Suwas S, Gottstein G, Kumar R. Mater Sci Eng A 2007;A471:1.
[22] Beausir B, Suwas S, Tóth LS, Neale KW, Fundenberger J-J. Acta Mater 2008;56:200.
[23] Agnew SR, Horton JA, Lillo TM, Brown DW. Scripta Mater 2004;5:377.
[24] Agnew SR, Mehrotra P, Lillo TM, Stoica GM, Liaw PK. Acta Mater 2005;53:3135.
[25] Choi WS, Ryoo HS, Hwang SK, Kwun SI, Chae SW. Metall Mater Trans A 2002;33A:973.
[26] Biswas S, Satyaveer Singh D, Suwas S. Mater Sci Forum 2008;584–586:343.
[27] Gottstein G. Physical foundations of materials science. Berlin Heidelberg New York: Springer Verlag; 2004. p. 224.
[28] Skrotzki W, Tamm R, Klemm R, Thiele E, Holste C, Baum H. Mater Sci Forum 2002;408–412:667.
[29] Shin DH, Kim I, Kim J, Kim YS, Semiatin SL. Acta Mater 2003;51:983.
[30] Skrotzki W, Kloden B, Lankau A, Chulist R, Kopylow V, Brokmeier HG. Arch Metall Mater 2008;53:29.
[31] Mathieu J-P, Suwas S, Eberhardt A, Tóth LS, Moll P. J Mater Proc Tech 2006;173:29.
[32] Bunge HJ. Texture analysis in materials science–mathematical methods. London: Butterworths; 1982.
[33] Oh KH, Cho JH, Kim DI. REDS software (Reprocessing of EBSD Data), Version 0.8.000. Seoul: Seoul National University; 2002.
[34] Beausir B, Tóth LS, Neale KW. Acta Mater 2007;55:2695.
[35] Molinari A, Canova GR, Ahzi S. Acta Metall 1987;35:2983.
[36] Lebensohn RA, Tomé CN. Acta Metall 1993;41:2611.
[37] Lebensohn RA, Tomé CN. VPSC code, Version 7, Los Alamos; 2006.
[38] Hutchinson JW. Proc. Royal Soc London A 1976;101:127.
[39] Tomé CN, Lebensohn RA, Kocks UF. Acta Metall Mater 1991;39:2667.
[40] Yapici GG, Karaman I. Mater Sci Eng A 2009;A 503:78.
[41] Skrotzki W, Kloden B, Hunsche I. Mater Sci Forum 2007;558–559:575.
[42] Suwas S, Kim DI. Mater Sci Forum 2007;558–559:1353.
[43] Skrotzki W, Scheerbaum N, Oertel CG, Brokmeier H-G, Suwas S, Tóth LS. Acta Mater 2007;55:2211.